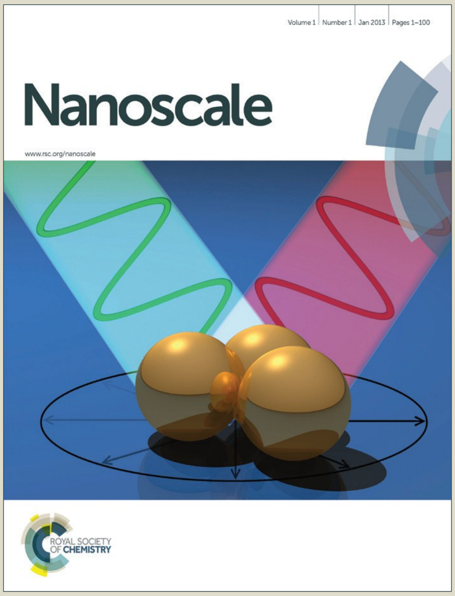
Volume 1 | Number 1 | Jan 2013 | Pages 1–100
Nanoscale
www.rsc.org/nanoscale
ROYAL SOCIETY OF CHEMISTRY

Journal name

PAPER

nReceived 00th January 20xx,
Accepted 00th January 20xx
DOI: 10.1039/x0xx00000x

www.rsc.org/

# Hierarchical $FeTiO_3$-$TiO_2$ hollow spheres for efficient simulated sunlight-driven water oxidation

Taoran Han,[a] Yajie Chen,[a] Guohui Tian,*[a,b] Jian-Qiang Wang,[c] Zhiyu Ren,[a] Wei Zhou[a] and Honggang Fu*[a]

Oxygen generation is the key step for the photocatalytic overall water splitting and considered to be kinetically more challenging than hydrogen generation. Here, effective water oxidation catalyst of hierarchical $FeTiO_3$-$TiO_2$ hollow spheres are prepared via two-step sequential solvothermal processes and followed by thermal treatment. The existence of effective heterointerface and built-in electric field in the surface space charge region in $FeTiO_3$-$TiO_2$ hollow spheres plays a positive role in promoting the separation of photoinduced electron-hole pairs. Surface photovoltage, transient-state photovoltage, fluorescence and electrochemical characterization are used to investigate the transfer process of photoinduced charge carriers. The photogenerated charge carriers in the hierarchical $FeTiO_3$-$TiO_2$ hollow spheres with a proper molar ratio display much higher separation efficiency and longer lifetime than those in the $FeTiO_3$ alone. Moreover, it is suggested that the hierarchical porous hollow structure can contribute to the enhancement of light utilization, surface active sites and material transportation through the framework walls. This specific synergy significantly contributes to the remarkable improvement of the photocatalytic water oxidation activity of the hierarchical $FeTiO_3$-$TiO_2$ hollow spheres under simulated sunlight (AM1.5).

## 1. Introduction

Recent Years, steadily growing energy crisis has directed a global trend toward sustainable development.[1-3] Access to alternative clean energy is expected to make considerable contribution. Solar induced water splitting has been considered as one of the most attractive routes because of its potential for hydrogen and oxygen production without the use of fossil fuel energy.[4-6] The major challenge for water splitting is the oxygen evolution, which is an uphill reaction involved a four-electron transfer process, so the research on the photocatalytic oxygen evolution has recently been intensified as it serves as the key step for the artificial overall water splitting.[7-10] Currently, most of the effective water oxidation catalysts contain noble metals iridium and ruthenium as active species, which limits their widespread application.[11-15] Considering the practical application, apart from simple metal oxides ($Fe_2O_3$ , $WO_3$, $MnO_x$,), complicated binary and ternary oxides, such as, Co-g-$C_3N_4$, $LaTiO_2N_{14}$, $RTiNO_2$, $Co_3O_4/SiO_2$, have also been investigated.[16-18] However, until now, the efficiency of photocatalytic water oxidation is still moderate, which extremely restricts its practical application. Thus, tremendous efforts are still needed to improve their catalytic performance.

In recent years, titanium based perovskite oxides such as $ATiO_3$ (A=Zn, Sr, Co, Fe and Ni) have been identified as a kind of significant photocatalyst for the photocatalytic degradation of toxic pollutants, photocatalytic hydrogen and oxygen production.[19-23] For example, $CoTiO_3$ could be regarded as visible light-driven photocatalyst for water oxidation.[24] $SrTiO_3$ was used as photocatalyst for photocatalytic hydrogen evolution.[25,26] $NiTiO_3$ and $FeTiO_3$ exhibited high visible light photocatalytic activity in removing organic pollutants.[27-30] But as far as we know, $FeTiO_3$ and its composites have not been applied for photocatalytic oxygen evolution from water splitting. Inspired by the previous studies about other titanium based perovskite oxides for photocatalytic water oxidation, it is expected to explore the synthesis and application of $FeTiO_3$ for photocatalytic water oxidation. Because the improved interface transfer rate of charge carriers can play a prominent role in promoting the water oxidation rate, coupling of $FeTiO_3$ with a wide bandgap semiconductor (e.g. $TiO_2$) with proper valence band position may expect to construct $FeTiO_3$-based heterostructure composites and improve the transfer of photogenerated holes from $FeTiO_3$ to the wide bandgap semiconductor, so contributing to the enhancement of photocatalytic oxidation ability.[31] It is known that morphology and structure are important factors influencing the photocatalytic water oxidation properties of semiconductor photocatalyst.[32] Owing to the special properties (low density, large surface area and high light-harvesting efficiency), hollow micro-/nano-structure offer some potential for photocatalytic application.[33] To this end, Wang and coworkers have carried out lots of significant works to synthesize hollow carbon nitride nanospheres to develop functional photosynthetic structures for solar energy application.[34] Motivated by the high photocatalytic performance of hollow spheres, it is expected to explore the synthesis of hierarchical $FeTiO_3$-$TiO_2$ hollow spheres to achieve enhanced photocatalytic water oxidation activity under simulated sunlight irradiation by reducing the recombination rate of the charge carriers, decreasing the energy barrier of the water oxidation kinetics, enhancing the light-harvesting efficiency, and increasing surface catalytic active sites.

In the present study, we summarized our recent efforts towards the facile synthesis and photocatalytic application of hierarchical $FeTiO_3$-$TiO_2$ hollow spheres. Different from the previously reported methods, hierarchical titanium-glycerolate-iron complex hollow sphere precursors were first prepared via two-step sequential solvothermal processes, then, after calcination, the hierarchical $FeTiO_3$-$TiO_2$ hollow spheres can be prepared. Changing the ratio of the molar of Ti and Fe added to the solution, the hierarchical $FeTiO_3$ hollow spheres can also be obtained. The novel hierarchical $FeTiO_3$-$TiO_2$ hollow spheres showed enhanced photocatalytic water oxidation performance and excellent recycling stability. We also demonstrated the well designed synergistic effects in the photocatalysts, including the semiconductor heterojunction effect, matched energy level position, as well as the special hierarchical hollow structural advantage, could efficiently promote the photogenerated charge carriers separation and transfer across the interfacial domain. As expected, the optimal hierarchical $FeTiO_3$-$TiO_2$ hollow spheres photocatalytic system exhibited ~2-fold enhancement in photocatalytic oxygen production as compared to pure $FeTiO_3$.

## 2. Experimental section

### 2.1 Preparation of $FeTiO_3$-$TiO_2$ hollow spheres

In the typical experiment, 0.7 mL Tetrabutyl titanate (TBOT) and 5mL glycerol (Gly) were dissolved in 25 mL ethanol to form a clear solution. Then the solution was transferred to a 50 mL Teflon-lined stainless steel autoclave. After which the autoclave was heated to 180°C, and keeping this temperature for 24 h. After the solvothermal reaction, the reactor was naturally cooled to room temperature. The obtained solid product was transferred into another 50 mL Teflon-lined stainless steel autoclave. Then, 0.8310 g $Fe(NO_3)_3{\cdot}9H_2O$, 3 mL glycerol and 25 mL ethanol were added to the autoclave to well mix the mixture. The autoclave containing mixture solution was then heated to 180 ℃ and maintained for 12 h. Subsequently, the autoclave was naturally cooled to room temperature. The precipitate was washed by absolute ethanol for three times and dried at 70 °C in air. The resulting green powders were calcined in static air at 550 °C for 6 h at a heating rate of 2 °C $min^{-1}$, and $FeTiO_3$-$TiO_2$ hollow spheres were obtained. Similarly, $FeTiO_3$ hollow spheres can be prepared by adjusting the mole ratio of Ti and Fe.

### 2.2 Characterization

Powder X-ray diffraction (XRD) data of the samples were recorded with Bruker D8 Advance using Cu Ka radiation source (40 kV, 44 mA). Scanning electron microscopy (SEM) characterizations were performed on a Hitachi S-4800 electron probe microanalyzer. Transmission electron microscopy (TEM) studies were carried out with a JEOL 2100 TEM microscope operated at 200 kV. XPS (X-ray photoelectron spectroscopy) analysis was performed on a VG ESCALABMK II with a Mg Kaachromatic X-ray source (1253.6 eV). UV-vis diffuse reflectance spectra (DRS) were determined by a UV-vis spectrophotometer (ShimadzuUV-2550). The $N_2$ adsorption–desorption isotherms of as-prepared samples were conducted by using a Micromeritics Tristar II. The fluorescence spectra (PL) of the samples at room temperature were characterized via the fluorescence spectrophotometer (F-7000, Hitachi, Japan). The excitation wavelength was 315 nm induced from a He-Cd laser source to excite the samples. The XAFS data at the Ti and Fe K3-edge were measured at room temperature in transmission mode at beamline BL14W1 of Shanghai Synchrotron Radiation Facility (SSRF), China.

### 2.3 Electrochemical test

Linear sweep voltammetry (LSV) and electrochemical impedance (EIS) experiments were obtained with a Versa STAT3 electrochemical workstation in a conventional three-electrode cell. FTO was the working electrode, Ag/AgCl (saturated KCl) was the reference electrode, and a platinum wire having 2 $cm^2$ of surface area served as the counter electrode. The working electrode was prepared on FTO glass that was cleaned by sonication in water, acetone, ethanol for 30 min respectively and dried at 333 K. Five milligrams of catalyst was mixed with 1 mL of ethanol by sonication to give a slurry mixture. The slurry was spread onto pretreated FTO glass. After air drying, the working electrode was further dried at 373 K for 2 h to improve adhesion. The electrolyte was 1 M KOH aqueous solution without additive (pH 14). The scan rate was 50 mV $s^{-1}$.The reference was calibrated against and converted to reversible hydrogen electrode (RHE). All the tests were carried out at room temperature (about 25 ℃).

### 2.4 Photocatalytic water oxidation test

The photocatalytic $O_2$ evolution from water was conducted in an online photocatalytic oxygen production system (AuLight, Beijing, CEL-SPH2N). For each reaction, 50 mg of catalyst powder was well dispersed in an aqueous solution (100 mL) containing $AgNO_3$ (0.01 M) as an electron acceptor. The reaction was carried out by irradiating the suspension with light from a 300 W Xe lamp (AuLight, CEL-HXF-300，Beijing) lamp with a working current of 15 A. The wavelength of the incident light was controlled by applying some appropriate long-pass cutoff filters. Prior to the reaction, the mixture was deaerated by evacuation to remove $O_2$ and $CO_2$ dissolved in water. Gas evolution was observed only under photoirradiation, being analyzed by an on-line gas chromatograph (SP7800, TCD, molecular sieve 5 Å, $N_2$ carrier, Beijing Keruida Limited).

Apparent quantum yield (A.Q.Y.) was measured using a 420 nm, 450 nm and 520 nm band-pass filter and an irradiate-meter, and calculated according to the following equation:

$$\text{A.Q.Y. (\%)} = \frac{\text{the number of reacted electrons}}{\text{the number of incident photos}} \times 100$$

$$= \frac{\text{the number of evolved } O_2 \text{ molecules} \times 4}{\text{the number of incident photos}} \times 100$$

### 2.5 Photocatalytic degradation test

The photodegradation experiments were performed in a slurry reactor containing 100 mL of 50 mg $L^{-1}$ 2, 4-dichlorophenol and 0.05 g of catalyst. A 300 W xenon lamp (Institute of Electric Light Source, Beijing) was used as the solar-simulated light source, and visible light was achieved by 420 nm cutoff filter. Prior to light irradiation, the suspension was kept in the dark under stirring for 30 min to ensure the establishing of an adsorption/desorption equilibrium. Adequate aliquots (5 mL) of the sample were withdrawn after periodic interval of irradiation, and centrifuged at

10000 rpm for 5 min, then filtered through a Milipore filter (pore size 0.22 mm) to remove the residual catalyst particulates for analysis.

In order to detect the active species during the photocatalytic reaction, isopropanol (IPA), ammonium oxalate (AO), benzoquinone (BQ) and $AgNO_3$ were added into the 2, 4-dichlorophenol solution dispersed with the $FeTiO_3$-$TiO_2$ heterostructures photocatalyst to capture hydroxyl radicals (•OH), holes ($h^+$), superoxide radicals (•$O_2^-$), and the electrons ($e^-$), respectively, followed by the photocatalytic activity test.

The electron spin resonance (ESR) technique (with DMPO) was used to detect the •$O_2^-$ radical species over the catalyst on a Bruker EMX-8/2.7 spectrometer by accumulating three scans at a microwave frequency of 9.85 GHz and a power of 6.35 mW. Before testing, DMPO was added to the suspension system, and then the system was irradiated by visible light using a halogen tungsten lamp with a UV cutoff filter ($\lambda > 400$ nm).

A total organic carbon (TOC) analyzer (Analytik Jena, Multi N/C 2100S, Germany) was employed for mineralization degree analysis of the dye solutions. Prior to injection into the TOC analyzer, the samples were filtrated with a Millipore filter. All experiments were carried out at least in duplicate. The reported values were within the experimental error range of ±3%.

## 3. Results and discussion

### 3.1. Structural and composition characterization

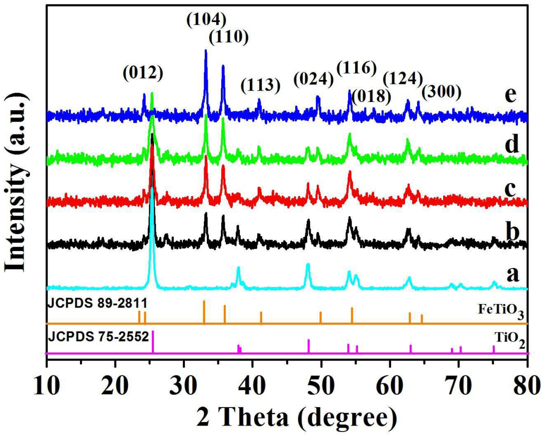

**Fig. 1** XRD spectra of the products prepared from different molar ratios of Ti and Fe, (a) 1:0, (b) 1:0.25, (c) 1: 0.5, (d) 1:0.75, (e) 1:1.

As shown in Fig. 1A, the typical characteristic diffraction peaks of anatase $TiO_2$ were detected at 2θ= 25.4° (101), 37.9° (004) and 48.1° (200) when no Fe salt was added in the reaction system. With the gradual introduction of the Fe salt, the XRD diffraction peaks of $FeTiO_3$ located at 2θ= 23.79° (012), 32.51° (104), 35.25° (110), 40.27 (113) and 53.02 (116) can be found in the different products.[29] Meanwhile, superimposition XRD patterns of $TiO_2$ and $FeTiO_3$ can be observed in the case of $FeTiO_3$-$TiO_2$ samples (curve b-d), which demonstrates the integration of these two compositions with high purity and good crystallization. Moreover, with the decrease of the molar ratio of Ti and Fe, the intensity ratio of XRD diffraction peaks of $TiO_2$ and $FeTiO_3$-$TiO_2$ also gradually decreased, indcating the increase of the $FeTiO_3$ content in the composites. When the molar ratio of Ti and Fe is 1:1, pure $FeTiO_3$ can be prepared.

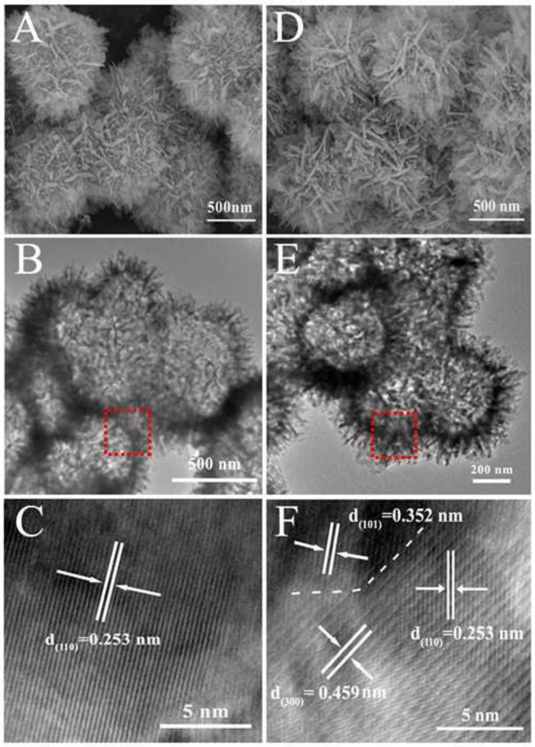

**Fig. 2** A, B, C are the SEM, TEM, HRTEM images of the $FeTiO_3$, respectively; D, E, F are the SEM, TEM, HRTEM images of the $FeTiO_3$-$TiO_2$ (Ti:Fe=1:0.75), respectively.

The morphology and microstructure of the $FeTiO_3$ and $FeTiO_3$-$TiO_2$ (Ti:Fe=1:0.75) composite were investigated by SEM and TEM. Fig. 2A and B shows the SEM and TEM images of the $FeTiO_3$. As expected, these spheres are hollow structure with particle diameters of about 0.5-1 μm. Meanwhile, as revealed in Fig. **2**D, E, the obtained $FeTiO_3$-$TiO_2$ also kept the hierarchical hollow structure, which clearly demonstrates the hollow structure having a shell consisting of interconnected nanoflakes with a thickness of about 15 nm. The nanopores in the shell proved to be interconnected from Fig. 2B and 2E. The specific surface area as large as about 45-65 $m^2$ $g^{-1}$ and a broad pore size distribution in hollow spheres measured from the $N_2$ adsorption–desorption curves (Fig. S1 and Table S1) also supported the TEM observation. The corresponding HRTEM image in Fig. 2C shows lattice fringes corresponding to the interplanar distance of 0.253 nm is ascribed to the (110) plane of rhombohedral $FeTiO_3$.[29] Fig. 2F depicts the spacings of adjacent lattice planes, which are consistent with the interplanar distance (0.253 nm) of the (110) plane of rhombohedral phase of $FeTiO_3$ and the interplanar distance (0.352 nm) of the (101) plane of anatase $TiO_2$, respectively, indicating the formation of heterojunction, which can benefit better charge separation and transfer within the hybrid structure compared with pure $FeTiO_3$ and $TiO_2$.

In order to disclose the morphology evolution and growth mechanism of the hierarchical $FeTiO_3$-$TiO_2$ hollow spheres, the SEM images of the $FeTiO_3$-$TiO_2$ precursors obtained at different reaction stages are shown in Fig. S2. The morphology evolution from nanoflowers to hierarchical hollow spheres can be clearly seen. Based on the above results, the possible growth pattern and formation mechanism of hierarchical $FeTiO_3$-$TiO_2$ hollow sphere precursors is shown in Scheme 1. The formation process includes two-step sequential solvothermal reactions. In the first solvothermal reaction process, amorphous titanium oxyhydrate nanospheres first formed through alcoholysis reactions between TBOT and ethanol, then glycerol gradually reacted with the formed titanium oxyhydrate to form titanium glycerolate (Ti-Gly) flower-like complexes by replacing the hydroxyls in titanium oxyhydrate. This is a dissolution-recrystallization growth process. With the reaction going on, the growth of thorn-like Ti-Gly complexes continued at the expense of the gradual dissolution of the solid spheres, and finally the product was entirely composed of the hierarchical flower-like nanostructure. The XRD pattern of the precursor is shown in Fig.S3a, which is in agreement with our previous report. [35] In the following solvothermal process, with the addition of iron salt, further solvothermal reaction led to the formation of Ti-Gly-Fe complexes from outer surface to inside, and the formed complexes diffused spontaneously toward the outer surface. The XRD patterns of the Fe-Gly-Ti complex in Fig. S3b,c exist several sharp peaks at low angle region and several weak ones at high angle region, which is similar to that of the reported metal glycerolate complexes.[35] Continuation of this process gradually dissolved the core spheres, sequentially formed hollow sphere structure. As a result from Ostwald ripening process, small nanoflakes initially formed on the surface of the hollow spheres and gradually grew up into ultrathin nanoflakes which are interlaced each other with thin edges and perpendicular to the surface of the hollow spheres. Finally, the hierarchical hollow sphere precursors were formed. After calcination, these precursors changed into $FeTiO_3$-$TiO_2$ composites without changing the hierarchical hollow sphere structure. Changing the molar ratio of Ti and Fe to 1:1, pure hierarchical $FeTiO_3$ hollow spheres can also be obtained.

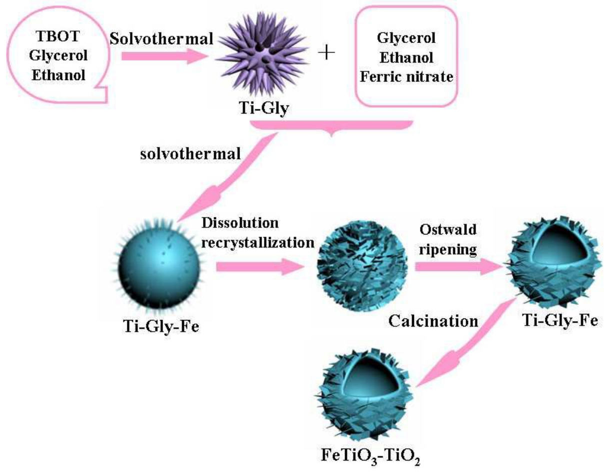

**Scheme 1** Schematic formation process of the hierarchical $FeTiO_3$-$TiO_2$ hollow spheres.

The $FeTiO_3$, $TiO_2$ and $FeTiO_3$-$TiO_2$ samples were characterized by X-ray absorption spectroscopy. The experimental XANES and EXAFS data of Fe K edge X-ray absorption spectra of $FeTiO_3$ and $FeTiO_3$-$TiO_2$ are plotted in Fig. 3C and 3D. The two samples bear a great similarity to each other. This show the load of $TiO_2$ particles doesn't change the structure of $FeTiO_3$. This might be ascribed to a concentration of $TiO_2$ that was too low to affect the environment of Fe in $FeTiO_3$. Fig. 3A displays the Ti K edge XANES of the different samples. The XANES spectrum of anatase $TiO_2$ is similar to those found in the literatures.[36,37] No significant differences are detected in the pre-edge region, suggesting a similar local symmetry in all of them. The Ti K-edge XANES spectrum of $FeTiO_3$-$TiO_2$ is similar to that of $FeTiO_3$, which suggests that $FeTiO_3$ is the main component in the $FeTiO_3$-$TiO_2$ composite, consistent with XRD results. Fig. 3B shows the Fourier Transform EXAFS spectra of Ti K-edge for different samples. The FT-EXAFS spectrum of the $FeTiO_3$-$TiO_2$ composite is similar with that of pure $FeTiO_3$. These results demonstrate that $FeTiO_3$ in $FeTiO_3$-$TiO_2$ composite is with a local structure of $FeTiO_3$. In comparison with pure $FeTiO_3$, there is a reduction in amplitude of FT peaks for $FeTiO_3$-$TiO_2$ composite. It was also observed that there is some difference $FeTiO_3$-$TiO_2$ and $TiO_2$ with regard to the bond distance of Ti to first-shell O atoms, which implies the existence of structural differences other than the differences in the Debye-Waller factor alone. However, the bond distances of Ti to first-shell O atoms in $FeTiO_3$-$TiO_2$ composite are nearly the same as that in pure $FeTiO_3$. This result indicates that the local structure of $FeTiO_3$ particles can be stabilized to some extent in the presence of $TiO_2$.

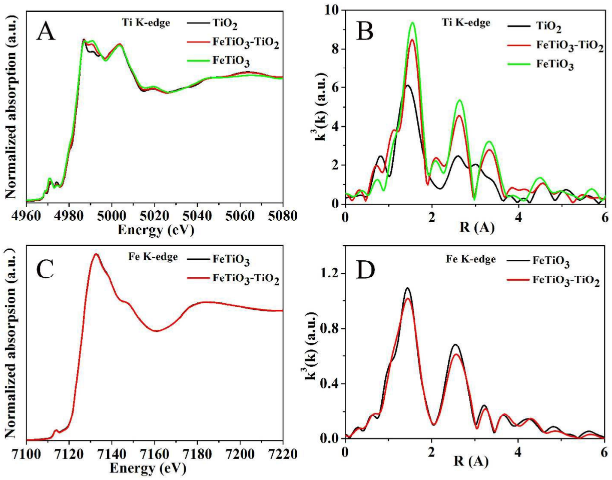

**Fig. 3** (A) and (C) are the X-ray absorption near-edge spectra (XANES) of Ti K-edge and Fe K-edge spectra of the samples, respectively; (B) and (D) are the corresponding extended X-ray absorption fine structure (EXAFS) spectra of Ti K-edge and Fe K-edge spectra of the samples, respectively.

The elemental compositions, chemical status and the interaction of $FeTiO_3$ and $TiO_2$ were further investigated by XPS. From XPS survey spectra of the samples in Fig. 4A, the existence of the peaks of Ti 2p, Fe 2p and O 1s can be confirmed in the $FeTiO_3$-$TiO_2$ composites. In Fig. 4B, the Fe $2p_{3/2}$ and Fe $2p_{1/2}$ peaks of $FeTiO_3$ can be identified at 711.01 eV and 724.61 eV, and slightly lower than those of $FeTiO_3$-$TiO_2$ located at 711.41 eV and 725.01 eV.[38] The Ti 2p spectrum from $TiO_2$ in Fig. 4C can be deconvoluted into two peaks centered at binding energies of 464.30 eV and 458.50 eV, which are assigned to Ti $2p_{1/2}$ and Ti $2p_{3/2}$ in the $Ti^{4+}$ oxidation state, respectively. For the $FeTiO_3$-$TiO_2$ composite, the corresponding Ti 2p peaks located at 464.14 eV and 458.34 eV. The slight shift of the peaks can be attributed to the interaction between $FeTiO_3$ and $TiO_2$ in the composite due to the formation of the heterostructure.[39,40] On the other hand, the O 1s XPS spectra in Fig. 4D of the samples can deconvoluted into two peaks. The first peak can be bound to lattice oxygen (O atoms bound to Ti and Fe). The second one is associated with hydroxyl species. The predominant O 1s peaks in $TiO_2$, $FeTiO_3$ and $FeTiO_3$-$TiO_2$ are 530.6, 530.1 and 529.6 eV, respectively. For the $FeTiO_3$-$TiO_2$ composite, the interaction between $FeTiO_3$ and $TiO_2$ resulted in the binding energy (530.1 eV) of O 1s in the $FeTiO_3$-$TiO_2$ composite is larger than that in the $FeTiO_3$ and lower than that in the $TiO_2$. The results indicated the heterostructure between $FeTiO_3$ and $TiO_2$ in the composite was formed upon calcination, and the electronic coupling between them was strengthened.

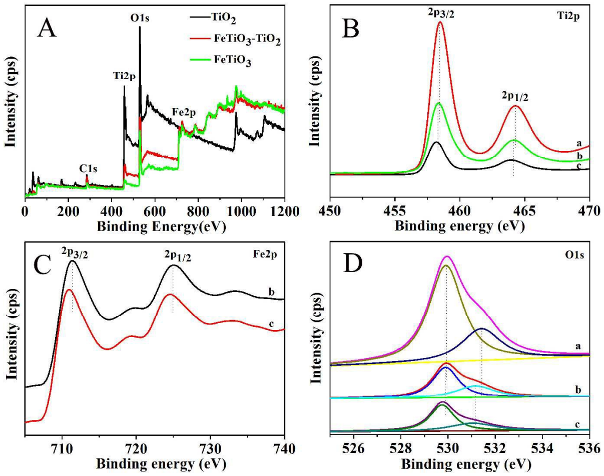

**Fig. 4** The survey XPS spectrum (A) and the high-resolution XPS scan of Fe 2p (B), Ti 2p (C) and O 1s peaks (D) of the different samples, (a) $FeTiO_3$-$TiO_2$ composite (Ti:Fe=1:0.75), (b) $FeTiO_3$, and (c) $TiO_2$.

The UV-vis diffuse reflectance spectra (DRS) of the as-prepared samples are shown in Fig. 5A. It can be seen that the absorption of the $TiO_2$ was located in the ultraviolet region, and the absorption wavelength was about 380 nm. However, compared with pure $TiO_2$, the absorption spectra of $FeTiO_3$ and hierarchical $FeTiO_3$-$TiO_2$ hollow spheres extend from UV to visible light region in contrast to the pure $TiO_2$. The extended photoresponse range, which came from $FeTiO_3$ with the bandgap of about 2.5 eV, accounted for the red shift as well. Moreover, a fair enhancement of the photo-absorption intensity of the $TiO_2$ in the range of 400-600 nm could be noticed with the increase of $FeTiO_3$ content, which indicating that the hierarchical $FeTiO_3$-$TiO_2$ hollow spheres have potential ability for visible-light photocatalysis.

The PL emission spectra are used to investigate the efficiency of charge carrier trapping, migration, transfer and separation and to understand the fate of photogenerated electrons and holes in semiconductor since PL emission results from the recombination of free carriers.[41,42] Fig. 5B presents a comparison of the PL spectra of the different samples. For $TiO_2$ and $FeTiO_3$-$TiO_2$ composites, the PL peaks at 450 and 530 nm are attributed to band edge free excitons.[43] A considerable fluorescence decrease (or quenching) is observed. The PL intensities order is opposite to the following photocatalytic activity studies. The suppression of PL implies either the slower recombination process with the longer decay lifetime or the faster migration process with the shorter decay lifetime for the photoinduced electrons.[44] This indicates that the $FeTiO_3$-$TiO_2$ composites have relative low recombination rate of electrons and holes under UV light irradiation. Generally, low recombination rate of electrons and holes is often associated with high photocatalytic activity.

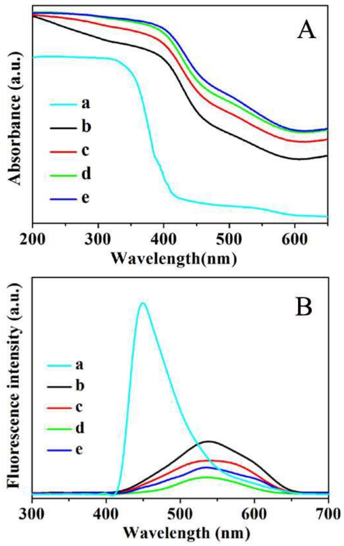

**Fig. 5** (A) UV–vis spectra and (B) room-temperature PL spectrum of (a)$TiO_2$, and $FeTiO_3$-$TiO_2$ composites prepared from different molar ratios of Ti and Fe, (b) 1:0.25, (c) 1:0.5, (d) 1:0.75, and (e) pure $FeTiO_3$.

### 3.2. Photogenerated charge properties

It is widely known in photocatalysis that the photocatalytic activity of material is closely related to the behavior of photogenerated charges.[45] Surface photovoltage spectroscopy (SPS) can effectively reflect the information about the separation and recombination of photoinduced charge carriers, so surface photovoltage technique was employed to characterize the behavior of photogenerated charge carriers in the system.[46] As shown in Fig. 6A, for single $FeTiO_3$ and $TiO_2$, the SPS response bands were obtained shows a positive signal in the range of 320−600 nm and 300−420 nm, respectively, which were due to the band−band transition (electrons transition from valence band to conduction band).[43] There was no any SPS response for $TiO_2$ under visible light irradiation. However, the $FeTiO_3$-$TiO_2$ composites displayed a similar SPS response range to $FeTiO_3$ suggesting that the photovoltage response of composite in the visible region mainly resulted from $FeTiO_3$. Under visible light irradiation, the response intensity of pure $FeTiO_3$ was weaker than the response intensity of the $FeTiO_3$-$TiO_2$ composites. Because the photovoltage response intensity was related to the charge separation efficiency, it signified that a stronger SPS response intensity, a higher separation efficiency of photoinduced charges. We speculated that there was an interfacial electric field in the $FeTiO_3$-$TiO_2$ composite formed during the calcination process. A positive signal means photoinduced holes accumulate at the surface, which indicates that the photoinduced holes move to the surface.[47] The response intensity of the $FeTiO_3$-$TiO_2$ composite (Ti:Fe=1:0.75) was higher than that of pure $FeTiO_3$ or $TiO_2$ because the existence of interfacial electric field enhances the separation of photoinduced charges.[47] Because the separation efficiency of photoinduced charge was one of the most important factors which influence the photocatalytic activity, hence, it was reasonable to deduce that the fast injecting of photogenerated holes from $FeTiO_3$ into $TiO_2$ contributed to the improvement of photocatalytic activity of the $FeTiO_3$-$TiO_2$ composites.

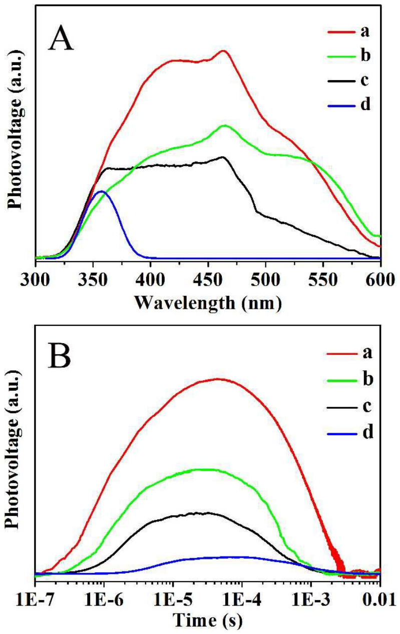

**Fig. 6** (A) Steady-state surface photovoltage spectra and (B) transient-state surface photovoltage responses of the different samples in air, (a) $FeTiO_3$-$TiO_2$ (Ti:Fe=1:0.75), (b) $FeTiO_3$-$TiO_2$ (Ti:Fe=1:0. 5), (c) $FeTiO_3$, and (d) $TiO_2$.

The corresponding transient-state photovoltage (TPV) responses of the samples shown in Fig. 6B indicated that the transient-state photovoltage response of the $FeTiO_3$-$TiO_2$ composite is obviously enhanced than that of pure $FeTiO_3$ and $TiO_2$. This is in good agreement with the steady-state photovoltage spectroscopy response. It is worthy of note that the lifetime of the photogenerated charge was also prolonged by several seconds. On the basis of the obviously enhanced surface photovoltage responses and the prolonged photogenerated charge lifetime, it is confirmed that the separation of photogenerated charge carriers of the $FeTiO_3$-$TiO_2$ composite could be considerably improved by coupling with a proper amount of nanocrystalline $TiO_2$.[47]

### 3.3. Photocatalytic activity for water oxidation

The photocatalytic performance of the as-prepared hierarchical $FeTiO_3$-$TiO_2$ hollow spheres was evaluated in an assay of the photocatalytic water oxidation reaction. As we know, the morphology and component of photocatalysts have great influence on their photocatalytic properties.[48] Herein, we first focus our studies on component-dependent photocatalytic oxygen evolution properties of the prepared samples. Fig. 7A shows the oxygen evolution on $FeTiO_3$, $TiO_2$, and $FeTiO_3$-$TiO_2$ catalysts. It is clear that the oxygen evolution rates of the composites are dramatically increased because of the existence of $TiO_2$. Moreover, the photocatalytic activity of oxygen evolution on the hierarchical $FeTiO_3$-$TiO_2$ hollow spheres is increased to a maximum when the elemental ratio of Ti to Fe is 1:0.75. The photocatalytic activity is increased by up to 2 times, compared with that for pure $FeTiO_3$ hollow spheres. This unambiguously indicates that the hierarchical $FeTiO_3$-$TiO_2$ hollow spheres can act as an efficient photocatalyst for oxygen evolution from water oxidation.

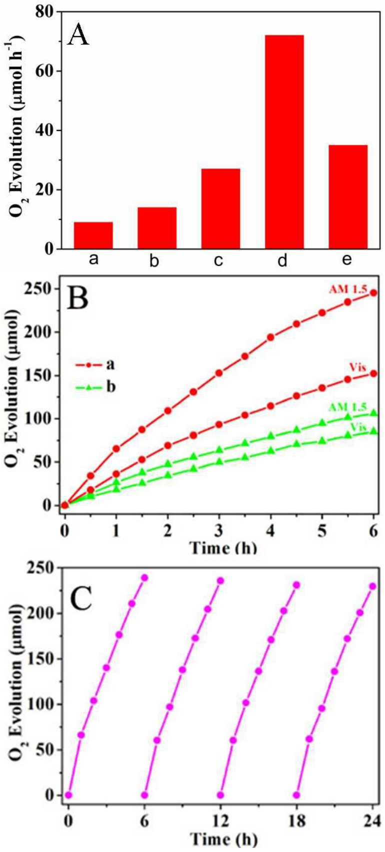

**Fig. 7** (A) The oxygen evolution of the different catalysts under simulated sunlight (AM 1.5) irradiation, (a) $TiO_2$, (b) $FeTiO_3$-$TiO_2$ (Ti:Fe=1:0.25), (c) $FeTiO_3$-$TiO_2$ (Ti:Fe=1:0.5), (d) $FeTiO_3$-$TiO_2$ (Ti:Fe=1:0.75), and (e) $FeTiO_3$ (Ti:Fe=1:1); (B) Time course of produced $O_2$ for the hierarchical $FeTiO_3$-$TiO_2$ hollow spheres (Ti:Fe =1:0.75) (a) and $FeTiO_3$ (b); (C) Cycling runs of the oxygen evolution of the hierarchical $FeTiO_3$-$TiO_2$ hollow spheres (Ti:Fe=1:0.75) under simulated sunlight (AM 1.5).

Moreover, long time course water oxidation experiments were carried out under simulated sunlight (AM 1.5) and visible light irradiation. As shown in Fig. 7B, when the reaction time is to 6 h, the oxygen evolution of the hierarchical $FeTiO_3$-$TiO_2$ hollow spheres (Ti:Fe =1:0.75) under AM 1.5 irradiation and visible light irradiation is 245 μmol and 151.8 μmol, respectively, indicating its high photocatalytic oxygen evolution ability. Meanwhile, it could be recognized that the photocatalytic activity was linear at an early period and gradually decreased after irradiation for about 2 h. It should be noted that this phenomenon is not related to bad stability but is caused by the light shielding effect of photodeposited Ag particles, as has been reported by pioneer studies.[49] In reuse test (Fig. 7C), although the rate of oxygen evolution is slightly decreased, the average oxygen evolution rate of the fourth cycle can reach 36 μmol h$^{-1}$. The results indicate the high activity and well reuse ability of $FeTiO_3$-$TiO_2$ for photocatalytic oxygen evolution. Since the $FeTiO_3$ hollow spheres and the $FeTiO_3$-$TiO_2$ hollow spheres have similar morphology and UV–vis absorption, their different photocatalytic oxygen evolution performance should be attributed to their component differences. The formation of the heterojunction between $FeTiO_3$ and $TiO_2$ in the $FeTiO_3$-$TiO_2$ hollow spheres effectively enhanced charge separation and transport, so improving the photocatalytic oxygen evolution performance.[50]

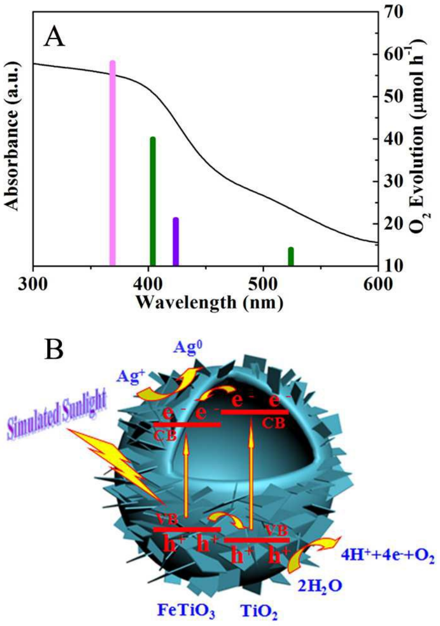

**Fig. 8** (A) The wavelength dependence of the oxygen evolution rates for the hierarchical $FeTiO_3$-$TiO_2$ hollow spheres (Ti:Fe=1:0.75) under single-wavelength light irradiation. (B) Schematic illustration for the enhanced photogenerated charge carriers separation and transfer in the hierarchical $FeTiO_3$-$TiO_2$ hollow spheres under simulated sunlight (AM 1.5).

We also evaluated the oxygen evolution rate of the hierarchical $FeTiO_3$-$TiO_2$ hollow spheres under different specific wavelength illuminations. As shown in Fig. 8A, the oxygen evolution rate of the hierarchical $FeTiO_3$-$TiO_2$ hollow spheres is associated with the DRS absorption spectra. The oxygen evolution rate of the hierarchical $FeTiO_3$-$TiO_2$ hollow spheres at 365 nm is 58 μmol h$^{-1}$, which is much larger than that at 420 (40 μmol h$^{-1}$), 450 (24 μmol h$^{-1}$), and 520 nm (14 μmol h$^{-1}$). It indicates that UV light is the main contributor to the high photocatalytic activity of the hierarchical $FeTiO_3$-$TiO_2$ hollow spheres under simulated sunlight (AM 1.5), and the photocatalytic oxygen evolution reaction is indeed promoted by the light irradiation. In visible light region, the apparent quantum yield (AQY) of $FeTiO_3$-$TiO_2$ is about 9.1% at 420 nm, 2.3% at 450 nm and 0.6% at 520 nm. The apparent quantum yield decreased with increasing the active wavelength and the lowest value of 0.2% was detected at 600 nm. It indicates the oxygen evolution reaction of the samples is associated with the DRS absorption spectra. As shown in Fig. 7C, the high oxygen yield with hierarchical $FeTiO_3$-$TiO_2$ hollow spheres was maintained even after the 4th run in 24 h. Their structure and morphology were indeed stable after repeated photocatalytic runs, and no significant change was observed (Fig. S4).

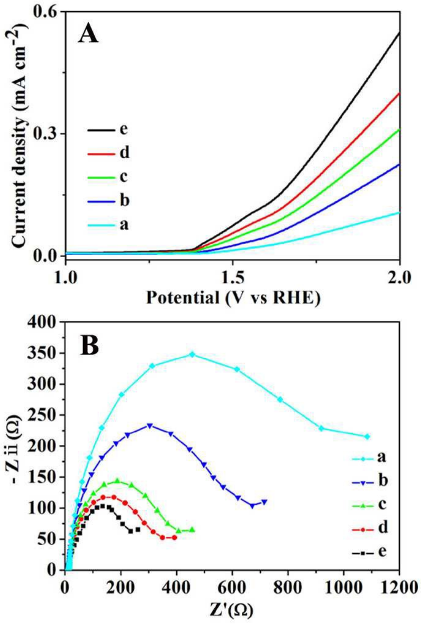

**Fig. 9** Linear sweep voltammetry (LSV) curves (A) and Nyquist plots of electrochemical impedance spectroscopy (B) recorded from different samples, (a) $TiO_2$, (b) $FeTiO_3$-$TiO_2$ (Ti:Fe=1:0.25), (c) $FeTiO_3$-$TiO_2$ (Ti:Fe=1:0.5), (d) $FeTiO_3$ (Ti:Fe=1:1), (e) $TiO_2$-$FeTiO_3$ (Ti:Fe=1:0.75).

For the hierarchical $FeTiO_3$-$TiO_2$ hollow spheres, under simulated sunlight irradiation, the photogenerated electrons in the valence bands (VB) of $FeTiO_3$ and $TiO_2$ transfer to the corresponding conduction bands, and then the photoexcited electrons in the conduction band (CB) of $TiO_2$ can transfer to the conduction band of $FeTiO_3$ due to the relatively high position. Meanwhile, the holes in the valence band of $FeTiO_3$ transfer to that of $TiO_2$.[29,30] These photogenerated charges transfer process reduces electron–hole recombination and maintains the requisite electron–hole populations required for photocatalytic reactions. Then the holes in the valence band of $TiO_2$ can participate the photocatalytic water oxidation reactions (Fig. 8B).[30] For photocatalytic water oxidation, the most important factor deciding the photocatalytic efficiency was likely the surviving fraction of long-lived photogenerated holes under photoirradiation.[51] In this photocatalytic oxidation process, more photoinduced holes accumulated on the surface of $FeTiO_3$-$TiO_2$, so the optimal $FeTiO_3$-$TiO_2$ hollow spheres exhibited significant enhancement on photocatalytic oxygen production. The inference can be evidenced by the above photoluminescence (Fig. 5B), surface photovoltage (SPS) and transient-state photovoltage (TPV) (Fig. 6) characterizations of the optimal $FeTiO_3$-$TiO_2$ (Ti:Fe=1:0.75) hollow spheres. The control experiment was also done to demonstrate the structure-induced enhancement of the photocatalytic performance of the hierarchical $FeTiO_3$-$TiO_2$ hollow spheres using the crushed sample as photocatalyst. It is clear that the hierarchical $FeTiO_3$-$TiO_2$ hollow spheres exhibited superior photocatalytic oxygen evolution activity over the crushed $FeTiO_3$-$TiO_2$ sample (Fig. S5). The observed enhancement of photocatalytic activity, in comparison with the crushed sample, could be attributed to more efficient multiple reflections of simulated sunlight (AM1.5) and the increased quantity of photogenerated electrons and holes available to participate in the photocatalytic water oxidation reactions.

To help clarify this issue, some photoelectrochemical characterisation was carried out. Fig. 9A shows a comparison of the polarization curves of the above three samples. The positive current in the range of 1.4−1.8 V vs RHE can be ascribed to oxygen evolution.[10] The current onset voltage of the $FeTiO_3$-$TiO_2$ hollow spheres in the dark is slightly shifted to lower potential after coupling with $TiO_2$. It is beneficial for promoting multiple-electron water oxidation kinetics and avoiding excessive driving potentials.[52] Moreover, it can be found that the photocurrent of the $FeTiO_3$-$TiO_2$ hollow spheres increased along with the introduction of the proper amount of $TiO_2$. The optimal hierarchical $FeTiO_3$-$TiO_2$ (Ti:Fe=1:0.75) hollow spheres exhibited the highest photocurrent density. Hence, it can be deduced that the hierarchical $FeTiO_3$-$TiO_2$ hollow spheres showed effective separation of photogenerated electrons and holes. We also carried out measurements of electrochemical impedance spectroscopy (EIS), which is an effective method for evaluating the internal resistances for the charge transportation process of electrode materials. The EIS Nynquist plots of the different samples are shown in Fig. 9B. It can be seen that the observed arc radii of the $FeTiO_3$-$TiO_2$ hollow spheres are slightly decreased after coupling with an appropriate amount of $TiO_2$, indicating its charge transfer resistance becomes somewhat smaller.[53] Both of the electrochemical results imply that the formation of heterojunction between $FeTiO_3$ and $TiO_2$ accelerates the charge carrier separation and migration, and thus promotes the heterogeneous photocatalytic water oxidation process.

Visible light photodecomposition of 2, 4-dichlorophenol was also performed to further prove the enhanced photocatalytic activity of the hierarchical $FeTiO_3$-$TiO_2$ hollow spheres and the role of the holes in the photocatalytic oxidation process. As shown in Fig. 10A, the hierarchical $FeTiO_3$-$TiO_2$ hollow spheres displayed significantly improved visible light photocatalytic performance compared to pure $FeTiO_3$ and $TiO_2$. In this photocatalytic reaction process, hole ($h^+$) and $•O^{2-}$ play decisive role in the performance enhancement, and both of them are the main oxidizing species. The ESR spin-trap technique with 5, 5-dimethyl-1-pyrroline N-oxide (DMPO) was employed to ascertain the $•O^{2-}$ species in the hierarchical $FeTiO_3$-$TiO_2$ hollow spheres degradation system in methanol solution under visible-light irradiation. As shown in Fig. S6, six characteristic peaks with intensity similar to that of DMPO−$•O^{2-}$ adducts were observed only under visible-light irradiation, which is consistent with the other studies for $•O^{2-}$ adduct.[54] These ESR results confirm that $•O^{2-}$ radicals exist in the hierarchical $FeTiO_3$-$TiO_2$ hollow spheres system under visible-light irradiation. In contrast, no such signals were detected in the dark. Meanwhile, the reactive species trapping experiments were also done. As shown in Fig. 10B, the addition of $AgNO_3$ and isopropanol (IPA) in the 2, 4-dichlorophenol solution has little effect on the photocatalytic activity of the hierarchical $FeTiO_3$-$TiO_2$ hollow spheres. Conversely, the photocatalytic degradation of 2, 4-dichlorophenol is obviously inhibited after the addition of ammonium oxalate (AO) and benzoquinone (BQ). Especially in the presence of ammonium oxalate (AO), the photocatalytic degradation of 2, 4-dichlorophenol is the worst. It indicated that hole ($h^+$) plays a major role for the degradation of 2, 4-dichlorophenol. In addition, the total organic carbon (TOC) measurement (Fig. S7) results proved that the hierarchical $FeTiO_3$-$TiO_2$ hollow spheres possessed very high mineralization ability. Together with the results of the photocatalytic oxygen evolution tests, the prepared hierarchical $FeTiO_3$-$TiO_2$ hollow spheres have great potential in solar energy capture and conversion.

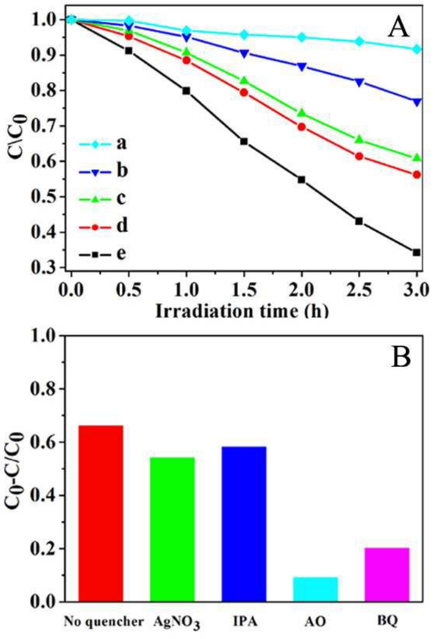

**Fig. 10** (A) Visible light photocatalytic degradation of 2, 4-dichlorophenol over (a) $TiO_2$, (d) $FeTiO_3$ and the hierarchical $FeTiO_3$-$TiO_2$ hollow spheres with different molar ratios of Ti:Fe, (b) 1:0.25, (c) 1:0.5, and (e) 1:0.75. (B) Comparison of photocatalytic activities of the hierarchical $FeTiO_3$-$TiO_2$ hollow spheres (Ti:Fe=1:0.75) with different scavengers during the photocatalytic reaction under 3 h visible light irradiation.

## 4. Conclusions

In summary, we have successfully synthesized hierarchical $FeTiO_3$-$TiO_2$ hollow spheres via two-step sequential solvothermal processes and followed calcination. The as-prepared hierarchical $FeTiO_3$-$TiO_2$ hollow spheres have shown enhanced photocatalytic water oxydation activity as well as excellent stability. This work confirms that the heterojunctions formed between these two kinds of semiconductors ($FeTiO_3$ and $TiO_2$) effectively promote the charge transfer. The photoinduced holes on the $FeTiO_3$ rapidly localizes to the $TiO_2$, and therefore promoting the oxygen evolution ability compared to pure

$FeTiO_3$ sample. Our results simultaneously suggest that the particular hierarchical porous hollow structure plays a positive role in enhancement of light utilization, effective increase in catalyst surface active sites and material transportation. It is believed that these research results can provide useful information for designing an optimal semiconductor that would combine the abilities of dissociating water molecules and possessing a proper band gap that absorbs solar light while remaining high stability.

## Acknowledgements

This research was supported by the National Natural Science Foundation of China (51272070, 21371053, 21376065, 21573062), Natural Science Foundation of Heilongjiang Province of China (E201455), Postdoctoral science-research developmental foundation of Heilongjiang province (LBH-Q13136). The authors thank beamline BL14W1 (Shanghai Synchrotron Radiation Facility) for providing the beam time.

## Notes

[a] *Key Laboratory of Functional Inorganic Material Chemistry, Ministry of Education of the People's Republic of China, Heilongjiang University, Harbin 150080 P. R. China*
[b] *Key Laboratory of Chemical Engineering Process & Technology for High-efficiency Conversion, College of Heilongjiang Province, School of Chemistry and Materials Science, Heilongjiang University, Harbin 150080, China.*
[c] *Shanghai Synchrotron Radiation Facility (SSRF), Shanghai Institute of Applied Physics, Chinese Academy of Sciences, Shanghai 201204, P. R. China*
*Corresponding author E-mail: tiangh@hlju.edu.cn; fuhg@vip.sina.com*, *Tel.: +86 451 8660 4330, Fax: +86 451 8667 3647*

† Electronic Supplementary Information (ESI) available: [details of any supplementary information available should be included here. See DOI: 10.1039/b000000x/

## References

1 J. Baxter, Z. X. Bian, G. Chen, D. Danielson, M. S. Dresselhaus, A. G. Fedorov, T. S. Fisher, C. W. Jones, E. Maginn, U. Kortshagen, A. Manthiram, A. Nozik, D. R. Rolison, T. Sands, L. Shi, D. Sholl and Y. Y. Wu, *Energy Environ. Sci.*, 2009, **2**, 559-588.
2 A. Kudo and Y. G. Miseki, Chem. *Soc. Rev.*, 2009, **38,** 253-278.
3 Y. Q. Zhong, K. Ueno, Y. Mori, X. Shi, T. Oshikiri, K. Murakoshi, H. Inoue and H. Misawa, *Angew. Chem*., 2014, **126,** 10518-10522.
4 R. M. Navarro, M. C. Alvarez-Galvan, J. A. V. De La Mano, S. M. Al-Zahrani and J. L. G. Fierro, *Energy Environ. Sci.*, 2010, **3,** 1865-1882.
5 (*a*) J. Q. Tian, H. Y. Li, A. M. Asiri, A. O. Al-Youbi and X. P. Sun, *Small,* 2013, **16,** 2709-2714; (*b*) G. Mattioli, P. Giannozzi, A. A. Bonapasta and L. Guidonili, *J. Am. Chem. Soc.,* 2013, **135,** 15353-15363.
6 (*a*) J. R. Ran, J. Zhang, J. G. Yu, M. Jaroniecc and S. Z. Qiao, *Chem. Soc. Rev.,* 2014, **43,** 7787-7812; (*b*) F. Jiao, H. Frei, *Energy Environ. Sci.,* 2010, **3,** 1018-1027.
7 N. Kaveevivitchai, R. Chitta, R. F. Zong, M. E. Ojaimi and R. P. Thummel, *J. Am. Chem. Soc.,* 2012, **134,** 10721-10724.
8 J. Rossmeisl, Z. W. Qu, H. Zhu, G. J. Kroes and J. K. Nørskov, *J. Electroanal. Chem.,* 2007, **607,** 83-89.
9 H. G. Casalongue, M. L. Ng, S. Kaya, D. Friebel, H. Ogasawara and A. Nilsson, *Angew. Chem. Int. Ed.,* 2014, **53,** 7169-9172.
10 G. G. Zhang, S. H. Zang and X. C. Wang, *ACS Catal.,* 2015, **5,** 941-947.
11 K. Maeda, *ACS Catal.,* 2013, **3,** 1486-1503.
12 Y. Miseki, S. Fujiyoshi, T. Gunji and K. Sayama, *Catal. Sci. Technol.,* 2013, **3,** 1750-1756.
13 Q. X. Jia, A. Iwase and A. Kudo, *Chem. Sci.,* 2014, **5**, 1513-1519.
14 T. Hisatomi, J. Kubota and K. Domen, *Chem .Soc. Rev.,* 2014, **43,** 7520-7535.
15 R. Cao, W. Z. Lai and P. W. Du, *Energy Environ. Sci.,* 2012, **5**, 8134-8157.
16 S. H. Porter, Z. G. Huang, S. X. Dou, S. Brown-Xu, A. T. M. G. Sarwar, R. C. Myers and P. M. Woodward, *Chem. Mater.,* 2015, **27**, 2414-2420.
17 (*a*) G. G. Zhang, C. J. Huang and X. C. Wang, *Small,* 2015, **11**, 1215-1221; (*b*) C. C. Li, Y. G. Guo and J. Vela, *ACS Catal.,* 2015, **5**, 1037-1044.
18 (a) D. C. Hong, Y. Yamada, T. Nagatomi, Y. Takai and S. Fukuzumi, *J. Am. Chem. Soc.,* 2012, **134**, 19572-19575.
19 J. B. Bellam, M. A. Ruiz-Preciado, M. Edely, J. Szade, A. Jouanneaux and A. H. Kassiba, *RSC Adv.,* 2015, **5**, 10551-10559.
20 Q. Kuang and S. H. Yang, *ACS Appl. Mater. Interfaces,* 2013, **5**, 3683-3690.
21 T. Surendar, S. Kumar and V. Shanker, *Phys. Chem. Chem. Phys*., 2014, **16**, 728-735.
22 L. Li, X. Liu, Y. L. Zhang, N. T. Nuhfer, K. Barmak, P. A.Salvador and G. S. Rohrer, *ACS Appl. Mater. Interfaces,* 2013, **5,** 5064-5071.
23 K. Wangkawong, S. Suntalelat, D. Tantraviwat and B. Inceesungvorn, *Mater. Lett.,* 2014, **133,** 119-122.
24 Y. Qu, W. Zhou and H. G. Fu, *ChemCatChem.,* 2014, **6,** 265-270.
25 (*a*) Q. Wang, T. Hisatomi, S. S. K. Ma, Y. B. Li and K. Domen, *Chem. Mater.,* 2014, **26,** 4144-4150; (*b*) L. L. Feng, X. X. Zou, J. Zhao, L. J. Zhou, D. J. Wan and X. Zhang, G. D. Li, *Chem. Commun.,* 2013, **49,** 9788-9790.
26 L. Q. Liu, P. Li, B. Adisak, S. X. Ouyang, N. Umezawa, J. H. Ye, R. Kodiyath, T. Tanabe, G. V. Ramesh and S. Ueda, *J. Mater. Chem. A,* 2014, **2,** 9875-9882.
27 Y. Qu, W. Zhou, Z. Y. Ren, S. C. Du, X. Y. Meng, G. H. Tian, K. Pan, G. F. Wang and H. G. Fu, *J. Mater. Chem.,* 2012, **22,** 16471-16476.
28 J. Y. Gan, X. H. Lu and Y. X. Tong, *Nanoscale,* 2014, **6,** 7142-7164.
29 Y. J. Kim, B. Gao, S. Y. Han, M. H. Jung, A. K. Chakraborty, T. Ko, C. Lee and W. I. Lee, *J. Phys. Chem. C,* 2009, **113,** 19179-19184.
30 (*a*) B. F. Gao, Y. J. Kim and A. K. Chakraborty, *Appl. Catal. B: Environ.,* 2008, **83,** 202-207; (*b*) Q. D. Truong, J. Y. Liu, C. C. Chung and Y. C. Ling, *Catal. Commun.,* 2012, **19,** 85-89.
31 H. L.Wang, L. S. Zhang, Z. G. Chen, J. Q. Hu, S. J. Li, Z. H. Wang, Z. S. Liu and X. C. Wang, *Chem. Soc. Rev.,* 2014, **43,** 5234-5244.
32 (*a*) X. Du and S. Z. Qiao, *Small,* 2015, **11,** 392-413; (*b*) H. Y. Liu, J. B. Joo, M. Dahl, L. S. Fu, Z. Z. Zeng and Y. D. Yin, *Energy Environ. Sci.,* 2015, **8,** 286-296; (*c*) J. Zhao,Y. C. Zou, X. X. Zou, T. Y. Bai, Y. P. Liu, R. Q. Gao, D. J. Wang and G. D. Li, *Nanoscale*, 2014, **6,** 7255–7262.
33 (*a*) Z. F. Jiang, W. Wei, D. J. Mao, C. Chen, Y. F. Shi, X. M. Lv and J. M. Xie, *Nanoscale*, 2015, **7,** 784-797; (*b*) Y. Z. Jiao, C. X. Peng, F. F. Guo, Z. H. Bao, J. H. Yang, L. Schmidt-Mende, R. Dunbar, Y. Qin

and Z. F. Deng, *J. Phys. Chem. C,* 2011, **115,** 6405-6409; (*c*) H. X. Li, Z. F. Bian, J. Zhu, D. Q. Zhang, G. S. Li, Y. N. Huo, H. Li and Y. F. Lu, *J. Am. Chem. Soc.,*2007, **129,** 8406-8407; (*d*) J. Qi, K. Zhao, G. D. Li, Y. Gao, H. J. Zhao, R. B. Yu and Z. Y. Tang, *Nanoscale,* 2014, **6,** 4072-4077; (*e*) Z. Wang, J. Hou, C. Yang, S. Jiao, K. Huang and H. Zhu, *Energy Environ. Sci.,* 2013, **6,** 2134-2144.

34 (*a*) J. H. Sun, J. S. Zhang, M. W. Zhang, M. Antonietti, X. Z. Fu and X. C. Wang, *Nat. Commun,* 2012*,* **3,** 1139-1146; (*b*) D. D. Zheng, C. Y. Pang, Y. X. Liu and X. C. Wang, *Chem. Commun.*, 2015, **51,** 9706-9709; (*c*) D. D. Zheng, C. J. Huang and X. C. Wang, *Nanoscale,* 2015, **7,** 465-470.

35 (*a*) C. Q. Wang, D. R. Chen and X. J. Jiao, *J. Phys. Chem. C,* 2009, **113,** 7714-7718; (*b*) D. Larcher, R. Sudant, R. Patrice and J. M. Tarascon, *Chem. Mater.,* 2003, **15,** 3543-3551; (*c*) G. H. Tian, Y. J. Chen, W. Zhou, K. Pan, C. G. Tian, X. R. Huang and H. G. Fu, *CrystEngComm,* 2011, **13,** 2994-3000.

36 M. Valant, I. Arcon, I. Mikulsk and D. Lisjak, *Chem. Mater.,* 2013, **25,** 3544-3550.

37 M. Valant, T. Kolodiazhnyi, I. Arcon, F. Aguesse, A. K. Axelsson and N. M. Alford, *Adv. Funct. Mater.* 2012, **22,** 2114-2122.

38 L. L. Peng, T. F. Xie, Y. C. Lu, H. M. Fan and D. *J.* Wang, *Phys., Chem. Chem. Phys.,* 2010, **12,** 8033-8041.

39 Y. Zhang, S. Lin, W. Zhang, H. Ge, G. Li, Y. Zhang, F. Y. Qi and X. M. Song, *RSC Adv.,* 2014, **4,** 3226-3232.

40 G. H. Tian, L. Q. Jing, H. G. Fu and C. G. Tian, *J. Hazard. Mater.,* 2009, **161,** 1122-1130.

41 S. Q. Liu, Z. Chen, N. Chen, Z. R. Tang and Y. J. Xu, *J. Phys. Chem. C,* 2013, **117,** 8251-8261.

42 Y. Xi, J. Zhou, H. Guo, C. Cai and Z. Lin, *Chim. Phys. Lett*., 2005, **412,** 60-64.

43 L. A. Gu, J. Y.Wang, H. Cheng, Y. Z. Zhao, L. F. Liu and X. J. Han, *ACS Appl. Mater. Interfaces,* 2013, **5,** 3085-3093.

44 Z. F. Bian, T. Tachikawa, P. Zhang, M. Fujitsuka and T. Majima, *J. Am. Chem. Soc.,* 2014, **136,** 458-465.

45 (*a*) L. Q. Jing, J. Zhou, J. R. Durrant, J. W.Tang, D. N. Liu and H. G. Fu, *Energy Environ. Sci.,* 2012, **5,** 6552-6558; (*b*) X. Wei, T. F. Xie, L. L. Peng, W. Fu, J. S. Chen, Q. Gao, G. Y. Hong and D. J. Wang, *J. Phys. Chem. C,* 2011, **115,** 8637-8642.

46 (a)Y. B. Luan, L. Q. Jing, Y. Xie, X. J. Sun, Y. J. Feng and H. G. Fu, *ACS Catal.,* 2013, **3,** 1378-1385; (b) L. J. Zhang, R. Zheng, S. Li, B. K. Liu, D. J. Wang, L. L.Wang and T. F. Xie, *ACS Appl. Mater. Interfaces,* 2014, **6,** 13406-13412.

47 (*a*) L. M. He, L. Q. Jing, Y. B. Luan, L. Wang and H. G. Fu, *ACS Catal.,* 2014, **4,** 990-998; (*b*) H. M. Fan, H. Y. Li, B. K. Liu,Y. C. Lu, T. F. Xie and D. J. Wang, *ACS Appl. Mater. Interfaces,* 2012, **4,** 4853-4857; (*c*) H. M. Fan, T. F. Jiang, H. Y. Li, D. J.Wang, L. L. Wang, J. L. Zhai, D. Q. He, P. Wang and T. F. Xie, *J. Phys. Chem. C,* 2012, **116,** 2425-2430.

48 Y. Y. Feng, H. J. Zhang, Y. Zhang, X. Li and Y. Wang, *ACS Appl. Mater. Interfaces,* 2015, **7,** 9203-9210.

49 (*a*) J. W. Shi, J. H. Ye, Q. Y. Li, Z. H. Zhou, H. Tong, G. C. Xi and L. J. Guo, *Chem. Eur. J.,* 2012, **18,** 3157−3162; (*b*) Z. G. Yi, J. H. Ye, N. Kikugawa, T. Kako, S. X. Ouyang, H. Stuart-Williams, H. Yang, J. Y. Cao, W. J. Luo, Z. S. Li, Y. Liu and R. L. Withers, *Nat. Mater.,*2010, **9,** 559−564; (*c*) D. J. Martin, N. Umezawa, X. W. Chen, J. H.Ye and J. W. Tang, *Energy Environ. Sci.,* 2013, **6,** 3380−3386.

50 C. H. Kuo, I. M. Mosa, A. S. Poyraz, Biswas, A. M. E-Sawy, W. Q. Song, Z. Luo, S. Y. Chen, J. F. Rusling and J. He, *ACS Catal.,* 2015, **5,** 1693-1699.

51 F. Amano, E. Ishinaga and A. Yamakata, *J. Phys. Chem. C,* 2013, **117,** 22584-22590.

52 (*a*) J. R. Ran, J. Zhang, J. G. Yu and S. Z. Qiao, *ChemSusChem*, 2014, **7,** 3426-3434. (*b*) T. Y. Ma, S. Dai, M. Jaroniec and S. Z. Qiao, J. Am. Chem. Soc., *2014,* **136,** 13925−13931.

53 S. Cruz-Manzo, R. Chen and P. Greenwood, *J. Electroanal. Chem*., 2015, **745,** 28-36.

54 (*a*) L.-S. Zhang, K.-H. Wong, H.-Y. Yip, C. Hu, J. M. Yu, C.-Y. Chan and P.-K. Wong, *Environ. Sci. Technol*., 2010, **44**, 1392−1398; (*b*) W. H. Ma, Y. P. Huang, J. Li, M. M. Cheng, W. J. Song and J. C. Zhao, *Chem. Commun.,* 2003, 1582−1583.